

## Observations of Strongly Modulated Surface Wave and Wave Breaking Statistics at a Submesoscale Front

TEODOR VREĆICA,<sup>a</sup> NICK PIZZO,<sup>a</sup> AND LUC LENAIN<sup>a</sup>

<sup>a</sup> *Scripps Institution of Oceanography, University of California, San Diego, La Jolla, California*

(Manuscript received 15 June 2021, in final form 5 October 2021)

**ABSTRACT:** Ocean submesoscale currents, with spatial scales on the order of 0.1–10 km, are horizontally divergent flows, leading to vertical motions that are crucial for modulating the fluxes of mass, momentum, and energy between the ocean and the atmosphere, with important implications for biological and chemical processes. Recently, there has been considerable interest in the role of surface waves in modifying frontal dynamics. However, there is a crucial lack of observations of these processes, which are needed to constrain and guide theoretical and numerical models. To this end, we present novel high-resolution airborne remote sensing and in situ observations of wave–current interaction at a submesoscale front near the island of O’ahu, Hawaii. We find strong modulation of the surface wave field across the frontal boundary, including enhanced wave breaking, that leads to significant spatial inhomogeneities in the wave and wave breaking statistics. The nonbreaking (i.e., Stokes) and breaking induced drifts are shown to be increased at the boundary by approximately 50% and an order of magnitude, respectively. The momentum flux from the wave field to the water column due to wave breaking is enhanced by an order of magnitude at the front. Using an orthogonal coordinate system that is tangent and normal to the front, we show that these sharp modulations occur over a distance of several meters in the direction normal to the front. Finally, we discuss these observations in the context of improved coupled models of air–sea interaction at a submesoscale front.


**KEYWORDS:** Currents; Wave breaking; Wind waves; Air–sea interaction

### 1. Introduction

Submesoscale fronts, jets, and eddies in the ocean are defined as currents with scales ranging from one-tenth to tens of kilometers (McWilliams 2016). These currents provide a pathway from quasi-two-dimensional mesoscale eddies, the main reservoir of kinetic energy in the ocean, to the fully three-dimensional dissipation scales (McWilliams 2016). Submesoscale variations have been shown to enhance mean heat fluxes at midlatitudes between the ocean and atmosphere (Su et al. 2018), potentially more than the change of air–sea heat fluxes due to climate change (Yu and Weller 2007). Furthermore, submesoscale motion can have strong horizontal divergences, which through mass conservation leads to upwelling and downwelling flows—facilitating exchanges between the atmosphere and the ocean. This has important biological implications by increasing both the production of phytoplankton and plankton biodiversity (Mahadevan 2016; Lévy et al. 2018). Submesoscale currents are also important for the dispersion of surface and near-surface pollutants, such as oil and plastics (Poje et al. 2014; D’Asaro et al. 2018). However, submesoscale currents are also difficult to measure, as they are generally too large for ship-based sampling and too small for orbital remote sensing products (McWilliams 2016). Therefore, there is a crucial need to observe submesoscale processes and in particular their interaction with other important features of the upper ocean.

High-resolution simulations have explored the complex life cycle of submesoscale features (e.g., Gula et al. 2014; McWilliams 2017; Sullivan and McWilliams 2018). Recently, the role of surface wave averaged effects, in particular the Stokes drift, has been explored in these models (Hamlington et al. 2014; Suzuki et al. 2016; McWilliams 2018). Wave breaking also generates currents (Rapp and Melville 1990; Melville et al. 2002; Pizzo et al. 2016; Deike et al. 2017) and the vertical vorticity induced by these finite crest breaking events (Peregrine 1999; Pizzo and Melville 2013) may lead to strong downwelling events through the so-called vortex force (Sullivan et al. 2007). However, the prescribed Stokes drift and breaking statistics are not well-constrained in these models (Sullivan et al. 2007). Furthermore, the spatial variability of the momentum flux is not necessarily realistic in these models, which often do not include the two-way coupling between the waves and underlying currents. This is particularly significant, as the spatial horizontal distribution of momentum flux is important for frontogenesis and can lead to the instability of submesoscale features [see Hoskins and Bretherton (1972) and Thomas and Lee (2005) for details]. These studies highlight the need to conduct high-resolution observations of the surface wave field and wave breaking statistics, including their spatial distribution, at submesoscale currents.

Surface waves can be strongly modulated by currents in the upper ocean, in particular near submesoscale fronts (Romero et al. 2017) where large horizontal gradients in the currents lead to strong wave refraction. A striking example is given by the recent study of Lenain and Pizzo (2021) that characterizes the intense transformation of surface waves by the currents induced by an internal wave train. Classical geometrical optics and wave action theories (Longuet-Higgins and Stewart 1964; Phillips 1966; Bretherton and Garrett 1968) show that it is

 Denotes content that is immediately available upon publication as open access.

Corresponding author: Teodor Vrećica, tvrecica@ucsd.edu

mostly shorter wave components which are strongly affected by submesoscale currents (McWilliams 2018). Furthermore, WKB theory predicts that vertical vorticity is responsible for creating ray curvature of these waves as they propagate over the currents (Kenyon 1971; Dysthe 2001), which has also been examined recently in the context of statistical theories (Arduin et al. 2017; Romero et al. 2020; Villas Bôas et al. 2020). However, it is still a topic of active debate as to the extent to which these WKB solutions hold for currents with large gradients (Shrira and Slunyaev 2014; Lenain and Pizzo 2021) or active two-way coupling with the currents (Pizzo and Salmon 2021), and there is an urgent need for more high-resolution spatio-temporal observations to test the fidelity of these theoretical and numerical predictions.

In recent years, the use of airborne remote sensing has enabled the detailed characterization of ocean surface properties, such as the directional properties of the wave field at resolutions down to  $O(0.1)$  m (see, e.g., Lenain and Melville 2017a,b; Lenain et al. 2019) and wave breaking statistics (Kleiss and Melville 2010; Sutherland and Melville 2013, 2015a). In Romero et al. (2017), airborne observations of the rapid evolution of the spectral properties of the surface wave field across the boundary of a submesoscale front were presented. They found that both wave and breaking statistics are strongly modulated through wave–current interaction processes. More recently, using a combination of in situ, airborne and orbital remote sensing approaches, Rascle et al. (2020) showed that submesoscale fronts can be very sharp ( $<50$  m), exhibiting very strong (horizontal) current shear. These studies are of tremendous interest but have lacked a detailed high-resolution description of the evolution of the wave field and wave breaking statistics in the immediate area of these fronts.

In this paper, using a unique set of airborne and in situ observations, we expand these studies by analyzing the directional and spectral properties of surface waves and wave breaking statistics across a submesoscale front located off Kaena Point on O’ahu, Hawaii. Additionally, surface currents, wave induced surface drift (Stokes and wave breaking), and momentum flux due to wave breaking are resolved as a function of distance from the frontal boundary at fine scale resolutions, which provides a rational framework for the investigation of these spatial distributions. The paper is structured as follow. In section 2 we introduce the variables and notation. In section 3 we describe the experiment and instrumentation. Shipborne observations, processing techniques, and an overview of the environmental conditions are given in section 4. Methods used in the analysis are presented in section 5. In section 6 we present the results, focusing on the evolution of surface wave properties, surface currents, and estimated momentum fluxes across the front. The results are discussed in section 7.

## 2. Background and definitions

### a. The sea surface wave spectrum

To analyze the properties of ocean surface waves, the surface elevation  $\eta$  can be approximated to first order as a linear superposition of sinusoidal waves, and can be characterized

statistically in terms of the directional ( $S$ ) and omnidirectional ( $\phi$ ) spectra, defined here as

$$\langle \eta^2 \rangle = \int_{k_{x,\min}}^{k_{x,\max}} \int_{k_{y,\min}}^{k_{y,\max}} S(k_x, k_y) dk_x dk_y = \int_{k_{\min}}^{k_{\max}} \phi(k) dk, \quad (1)$$

where  $\langle \rangle$  represents an averaging operation over the area for which the spectra are computed,  $k_x$  and  $k_y$  are the wavenumbers in the  $x$ - and  $y$ -axis direction, and  $k$  is the modulus of the wavenumber, i.e.,  $k = |\mathbf{k}| = \sqrt{k_x^2 + k_y^2}$ . Here,  $k_{x,\max}$  and  $k_{y,\max}$  are the largest resolved wavenumbers in the  $x$  and  $y$  direction. Similarly  $k_{x,\min}$  and  $k_{y,\min}$  are the smallest wavenumbers resolved in the  $x$  and  $y$  direction. We define  $k_{\max} = \sqrt{k_{x,\max}^2 + k_{y,\max}^2}$  and  $k_{\min}$  is the smallest modulus wavenumber resolved in our measurements.

Irrotational deep-water surface gravity waves have particle trajectories that are not closed, which leads to a net drift in the direction of the wave propagation, known as the Stokes drift (Phillips 1966). Following Kenyon (1969), the Stokes drift  $\mathbf{U}_s$  at the surface is computed from the directional wave spectrum  $S$ ,

$$\mathbf{U}_s = 2 \int S(\mathbf{k}) \sqrt{gk} \mathbf{k} d\mathbf{k}, \quad (2)$$

assuming a linear deep water dispersion relation. Note that Breivik et al. (2016), Pizzo et al. (2019), and Lenain and Pizzo (2020) have examined the contribution of various ranges of the spectrum (e.g., the equilibrium and saturation ranges; see Phillips 1985; Lenain and Melville 2017b) to the Stokes drift. There, they found that the saturation range (i.e., shorter waves) can contribute significantly to the total Stokes drift, highlighting the importance of high-resolution measurements of the surface wave field to properly resolve this important bulk scale quantity.

### b. Wave breaking statistics

To characterize properties of wave breaking near the front, following Phillips (1985) we define the breaking distribution as the average length of breaking crests with speed  $\mathbf{c}_b$  in the range  $(\mathbf{c}_b - \Delta\mathbf{c}_b/2, \mathbf{c}_b + \Delta\mathbf{c}_b/2)$  per unit surface area  $A$ , such that (Kleiss and Melville 2010)

$$\Lambda(\mathbf{c}_b) = \frac{1}{A\Delta\mathbf{c}_b} \sum_n \left( L_n \left| \mathbf{c}_b - \frac{\Delta\mathbf{c}_b}{2} < \mathbf{c}_{b,n} < \mathbf{c}_b + \frac{\Delta\mathbf{c}_b}{2} \right. \right), \quad (3)$$

where  $L_n$  is the length of actively breaking crest element, and  $\mathbf{c}_{b,n}$  is the velocity of the breaker element under consideration.

The utility of Phillips’s approach is that the spectral moments yield physically important variables. For example, the fourth moment of  $\Lambda(\mathbf{c}_b)$  yields the momentum flux induced by breaking waves,  $\mathbf{M}$ , defined as

$$\mathbf{M} = \frac{\rho_w}{g} \int b c_b^3 \mathbf{c}_b \Lambda(\mathbf{c}_b) d\mathbf{c}_b, \quad (4)$$

where  $\rho_w$  is the water density,  $g$  is the gravitational constant, and  $b$  is a parameter determining the strength of wave breaking (Drazen et al. 2008; Romero et al. 2012). To compute  $b$  we follow the procedure outlined in Romero et al. (2012). Note, Sutherland and Melville (2013) and Sutherland and Melville (2015a) used this formulation to compare the momentum flux



FIG. 1. An observation of enhanced wave breaking along a submesoscale ocean front, as recorded by a handheld digital single-lens reflex (DSLR) camera on 17 Apr 2018 near Kaena Point, O‘ahu, Hawaii. Notice the abrupt change between nonbreaking and breaking waves. The horizontal and vertical scales of this photograph are a few hundred meters. Wind direction and the direction of true north are roughly estimated in the photo.

from the wind to the water column with the momentum flux lost by the wave field and found that for waves with wave age ( $c_p/u_*$ ) of less than 50 the budget was approximately closed. Furthermore, these authors examined the energy dissipation rate through this formulation and compared the results to subsurface measurements of the dissipation rates, finding relatively good agreement.

Next, Pizzo et al. (2019) showed that the breaking induced drift  $U_b$  (Deike et al. 2017; Lenain et al. 2019; Sinnis et al. 2021) is computed from the third moment of the  $\Lambda(c_b)$  distribution. The value of the drift at the surface is defined as

$$U_b = \alpha \int (S - S_0) c_b \frac{c_b^2}{g} \Lambda(c_b) dc_b, \quad (5)$$

where  $S$  is the characteristic slope of the wave packet,  $S_0$  the breaking threshold,  $c_b$  the wave breaker velocity, and  $\alpha = 9$  is a constant found from the numerical simulations of Deike et al. (2017) and corroborated by the laboratory experiments of Lenain et al. (2019) and Sinnis et al. (2021).

Pizzo et al. (2019) examined the speed of the breaking induced drift versus the Stokes drift over a range of environmental conditions. For wind speeds ranging from 1.6 to 16 m s<sup>-1</sup>, significant wave heights in the range of 0.7–4.7 m, and wave ages ranging from 16 to 150, the author’s found that the breaking induced drift may be up to 30% of the Stokes drift.

Finally, the relationship between breaking crest velocity and wave phase velocity has been explored in numerous studies (see, e.g., Stansell and MacFarlane 2002). Following Romero et al. (2012), we assume here that the breaking crest velocity is equal the wave phase velocity (see also Sutherland and Melville 2013, 2015a).

### 3. Experiment and instrumentation

The experiment was conducted near Kaena Point on the island of O‘ahu, Hawaii, in April 2018. The Scripps Institution of Oceanography (SIO) Modular Aerial Sensing System (MASS; see Melville et al. 2016) airborne instrument was installed on a Cessna 206 operated by Williams Aerial Inc. The MASS was used to retrieve sea surface topography and collocated georeferenced aerial imagery (visible, infrared, and hyperspectral). While the present study was not part of the scientific objectives of the original project, a serendipitous observation of a line of a persistent enhanced breaking (see Fig. 1) during one of the flights led us to dedicate a portion of a flight to observing the modulation of surface wave properties across this front, on 17 April 2018. Several years after conducting these airborne observations, we discovered that the R/V *Ka‘imikai-O-Kanaloa* was also fortuitously present in the area, within a few hours of our flight time, while in transit to the Hawaii Ocean Time series (HOT) site, in support of a completely unrelated campaign (KOK1801; Rolling Deck to Repository 2019). Data collected from the ship are included in the analysis.

The MASS is a portable airborne remote sensing instrument (see Melville et al. 2016) developed in the Air–Sea Interaction Laboratory at the Scripps Institution of Oceanography. For this experiment, the MASS was equipped with a Riegl VQ-820G bathymetric lidar. Note that, although this model is designed for bathymetric surveys, it is also capable of collecting sea surface topography (multireturn waveform lidar). From the obtained georeferenced 3D lidar point clouds, datasets were regridded, with a discretization step of  $dx = dy = 0.25$  m. Aerial visible, hyperspectral, and infrared imagery were obtained with an IO Industries Flare 12M125-CL

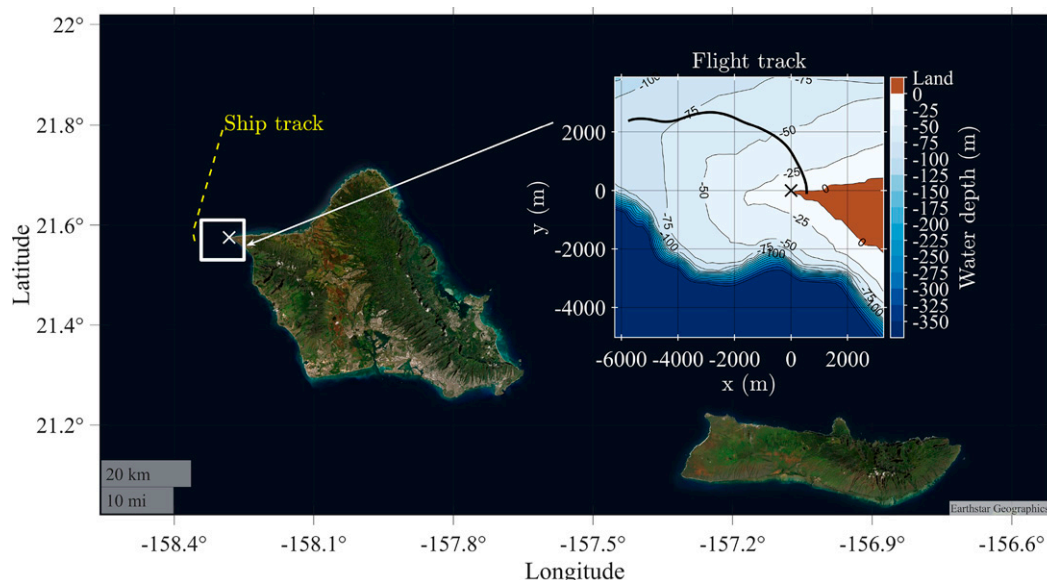


FIG. 2. An overview of the experiment site near Oahu, Hawaii. The white rectangle indicates the measurement area and is shown in more detail in the subfigure. The dashed yellow line indicates the research vessel track—with the vessel crossing Kaena Point approximately 1 h prior to the arrival of the plane. The subfigure also shows the flight track in black, overlaid over bathymetry contours, with  $dx = dy = 50$  m resolution.

camera ( $4096 \times 3072$  pixel resolution, 10 bit, 5-Hz sampling rate), a Specim AisaKESTREL 10 hyperspectral camera operating in the 400–1000-nm spectral range (1024 pixel cross-track resolution), and a FLIR SC6700SLS longwave infrared (IR) camera ( $640 \times 512$  pixel resolution, 50-Hz sampling rate), respectively. Portions of the visible band images affected by sun glint were discarded in the analysis. Vignetting effects were corrected by equalizing mean background brightness intensity and its standard deviation. Finally, these images were georeferenced with a discretization step of  $dx = dy = 0.2$  m.

A Novatel SPAN LN200 Inertial Measurement Unit (IMU) coupled to a ProPak6 GPS receiver was used to produce aircraft trajectory information (altitude and position) needed for georeferencing the lidar point cloud and imagery. Trajectory information from the GPS-IMU was postprocessed using Novatel Waypoint Inertial Explorer software. Visible imagery was processed using the Trimble INPHO software suite.

The R/V *Ka'imikai-O-Kanaloa* (now retired) was a 221-ft-long vessel, owned and operated by the University of Hawaii Marine Center. It was equipped with a Seabird SBE-21 analog thermosalinograph and SeaBird SBE-3S remote temperature sensor to sample salinity and water temperature at 4-m depth. The wind speed and direction were measured from a RM Young 5106 anemometer, mounted on a pole 13 m above the mean sea level. Finally, current profiles were measured from a Teledyne Workhorse 300-kHz ADCP (acoustic Doppler current profiler).

#### 4. Observations

Figure 1 shows a line of enhanced breaking observed at 0323 UTC 17 April 2018 from the cockpit of the aircraft. During this flight, the plane was flying at an altitude of

approximately 340 m above mean sea level, with a speed of about  $58 \text{ m s}^{-1}$ . Tracks of the aircraft and of the research vessel (within 1 h of the flight time) are shown in Fig. 2, overlaid over bathymetry contours (50 m horizontal resolution). At that time, the R/V *Ka'imikai-O-Kanaloa* was traveling approximately to the north, a few kilometers west of the flight track. Kaena Point ( $21.57515^\circ\text{N}$ ,  $158.28174^\circ\text{W}$ ) is chosen as the origin for the data transformation into a Cartesian coordinate grid. A simplified sketch showing the observed front, wind direction, and estimated currents (see section 5d for details), is given in Fig. 3.

##### a. Shipborne observations

Observations of near-surface water temperature, salinity, current profiles, wind speed and direction are shown in Fig. 4

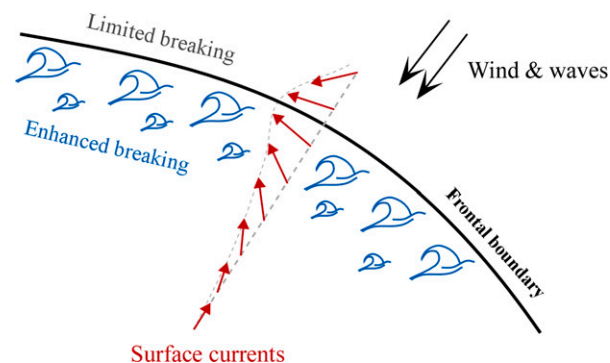


FIG. 3. Conceptual schematic of wave–current interaction processes occurring near the frontal boundary. Note the steepening of the surface wave field on one side of the front leading to enhanced breaking.



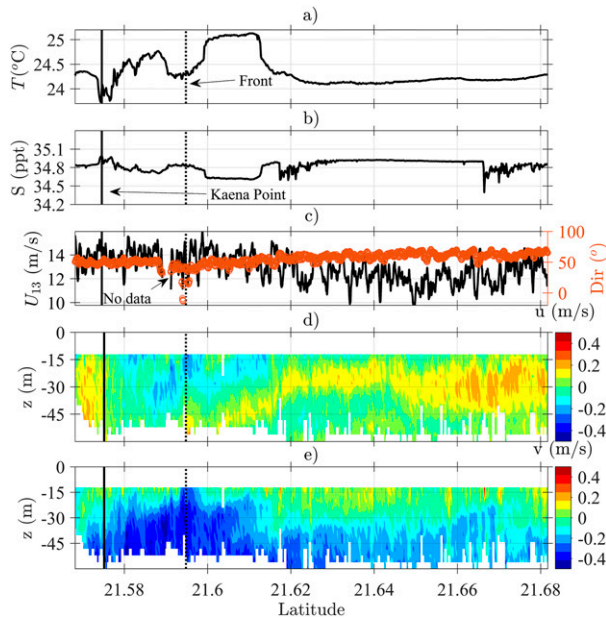


FIG. 4. Ocean and wind data measured by the R/V *Ka'imikai-O-Kanaloa*, as a function of latitude. The vertical solid line indicates position of Kaena Point (21.575° latitude), and the dashed vertical line indicates the position of the observed submesoscale current. (a) Water temperature, (b) salinity, (c) wind speed (black line), and mean wind direction (red points, meteorological direction convention). The empty portion of data corresponds to a fast change of course by the ship, which contaminated that portion of data. We also show (d) zonal and (e) meridional velocities as a function of depth. The shallowest resolved depth is  $d = 12$  m.

as a function of latitude, starting 1 h prior to the flight time. The latitude of Kaena Point and the submesoscale front observed by the aircraft are also shown. The wind speed and direction (13-m elevation) were relatively constant throughout the observation period, with an average magnitude of approximately  $12.9 \text{ m s}^{-1}$  and mean wind direction of  $55^\circ$  (coming from true north). This implies that the line of breaking observed from the aircraft is not associated with a rapid change in wind forcing that could occur in the wake of an island.

Both near-surface observations (temperature and salinity) and current profiles show the presence of a submesoscale feature, about 1 km wide, in the vicinity of the latitude of the front observed by the aircraft. At the frontal boundary, we find sharp gradients of temperature (up to  $0.5^\circ\text{C}$  in less than 100 m), and currents reaching magnitudes of up to  $0.4\text{--}0.5 \text{ m s}^{-1}$  (Figs. 4d,e). This submesoscale feature and temperature front are likely associated with tidally driven flow as the structure extends to significant depth (Srinivasan et al. 2019). Note that the locations (latitude) of the front captured from the aircraft and the ship do not precisely match, as the ship data near the front was collected a few kilometers away from that of the plane, and approximately 45 min prior, and we expect some meandering of the frontal boundary, as the Reynolds number of the flow associated with the current

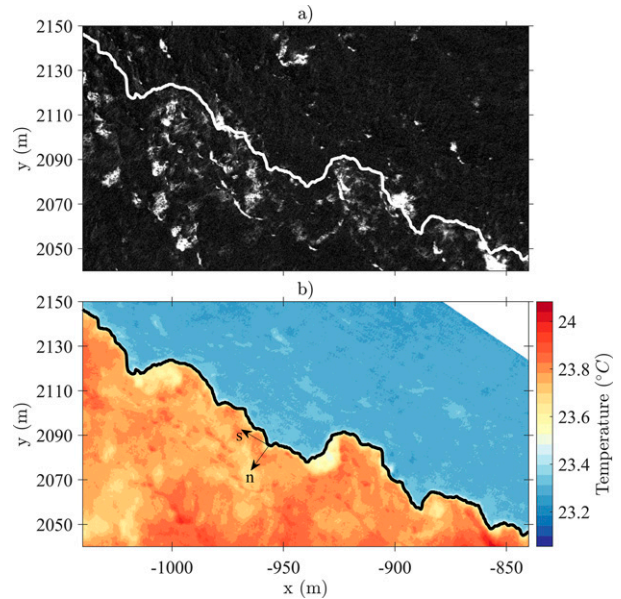


FIG. 5. (a) A georeferenced portion of the monochrome 16 bit image, recorded by the downward looking MASS camera. The white line represents the boundary of the temperature front. The whitecap coverage (due to air-entraining breaking waves) is undergoing a substantial amplification, coinciding with the change in SST. (b) A georeferenced infrared image for the same area as (a). Note the sharpness of transition between the warm and cold areas. The white area in the upper-right corner represents a region for which no infrared imagery was available.

implies fully turbulent motion. The shedding of vortices from the island is also a topic of considerable interest (Srinivasan et al. 2019), but falls outside of the scope of the current manuscript.

#### b. Remote sensing of ocean surface properties

Figure 5 shows a subset of georeferenced infrared and visible imagery collected from the MASS at the front. We find a sharp transition of sea surface temperature (SST) and wave breaking conditions over a very short distance, i.e., a few meters, which is quite remarkable. The SST is used to compute the frontal boundary using a  $23.5^\circ\text{C}$  threshold, shown in both subplots.

An overview of temperature and whitecap coverage is given for the entire surveyed area in Fig. 6. The submesoscale front extends for more than 4.5 km, with the warmer side of the front to the south, and the colder side to the north. Whitecap coverage is defined as the portion of the surface exceeding a set brightness threshold (see Callaghan and White 2009; Kleiss and Melville 2010, and the appendix for details). It is computed here using  $40 \times 40$  m segments of ocean surface observed from the MASS visible imagery, small enough to characterize spatial variability near the front (Fig. 6a).

We find a rapid increase in whitecap coverage across the front, by up to an order of magnitude, on the southern (warmer)

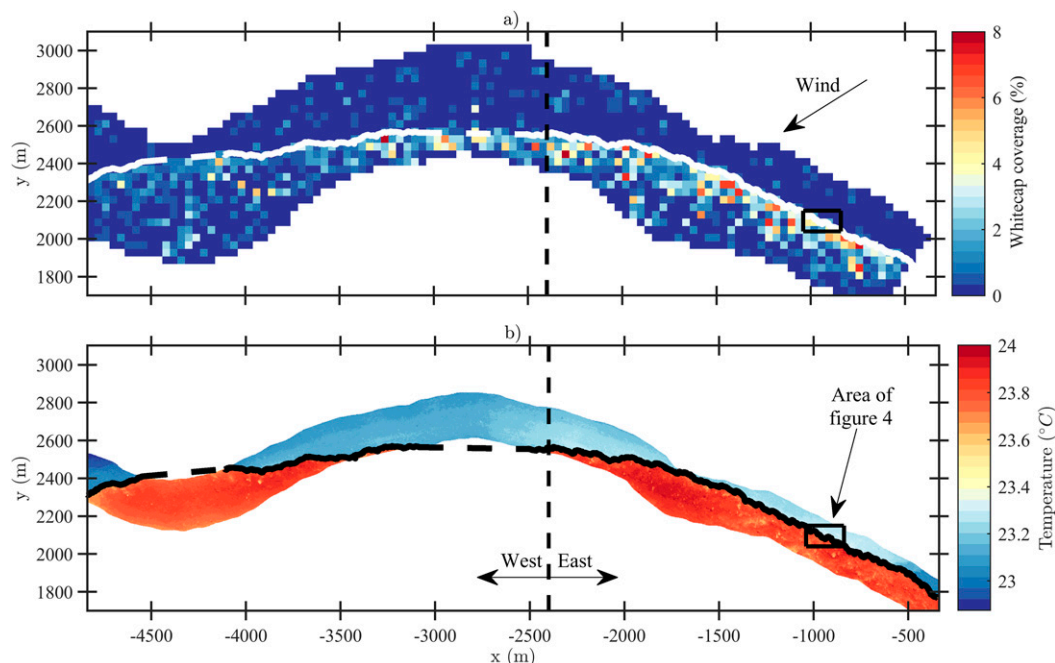


FIG. 6. An overview of the area. (a) Whitecap coverage, calculated in  $40 \times 40$  m cells, and (b) a mosaic of IR images are shown. The dashed vertical line indicates separation of front into two different areas at  $x = -2400$  m (east and west). The white lines in (a) and black lines in (b) indicate the position of the front, where dashed lines represent areas with no IR images (linear interpolation is used to draw these dashed lines). Due to its spatial variability, the front is divided into two areas east and west. The black box represents area of Fig. 5

side of the front along its entire length. Note, the largest values are found near the frontal boundary ( $<100$  m from the front).

To account for the front changing orientation with respect to the wind and wave direction (which are predominantly coming from the northwest) in our observations, two areas, designated as east ( $x > -2400$  m) and west ( $x < -2400$  m), are considered in the analysis.

The frontal boundary in the east area is oriented  $115^\circ$  from true north, while west area is oriented  $90^\circ$  from true north. Most of the subsequent analysis focuses on the east portion of the front where we experienced the largest wave breaking enhancement. Data close to shore, with depth less than 50 m, are discarded in the analysis to avoid potential bathymetric effects (e.g., refraction, shoaling, depth induced breaking).

To investigate the spatial evolution of SST and wave breaking near the front, we project these observations into a new coordinate system  $(x, y) \rightarrow (s, n)$ , where  $s$  is the tangent and  $n$  the normal direction along the front. The spatial evolution of variables is defined as a function of distance  $n$  from the front, as illustrated in Fig. 5b. The south side of the frontal boundary (warm area) corresponds to positive  $n$  values.

Figure 7 shows whitecap coverage  $W$  and SST averaged over both areas east and west using the new coordinate system. The warmer side of the front exhibits enhanced breaking as compared to the colder side, with the largest increase in whitecap coverage (by an order of magnitude) occurring within approximately 10 m of the frontal boundary (for both east

and west sections). Note the sharp “step-like” temperature gradient (over less than 10 m); such sharp transitions have only very recently been observed (Romero et al. 2017; Rascole et al. 2020).

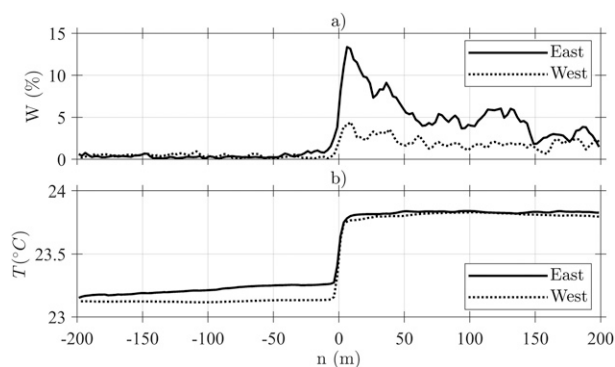


FIG. 7. Sea surface parameters as a function of distance from the front boundary, shown for east portion ( $x < -2400$  m) by a solid line, and for west portion by a dashed line. Results are presented for (a) whitecap coverage (fraction of surface covered by whitecaps), and (b) mean temperature. Our natural coordinate system, based on tangent and normal directions to the front, are such that  $n > 0$  indicates the south side of the front, and vice versa. Both east and west sections of the front show similar properties—characterized by a sharp transition at the frontal boundary—although the amplification of whitecap coverage is more severe for the east portion. Changes of temperature and of whitecap coverage are found to be well correlated at the frontal boundary.

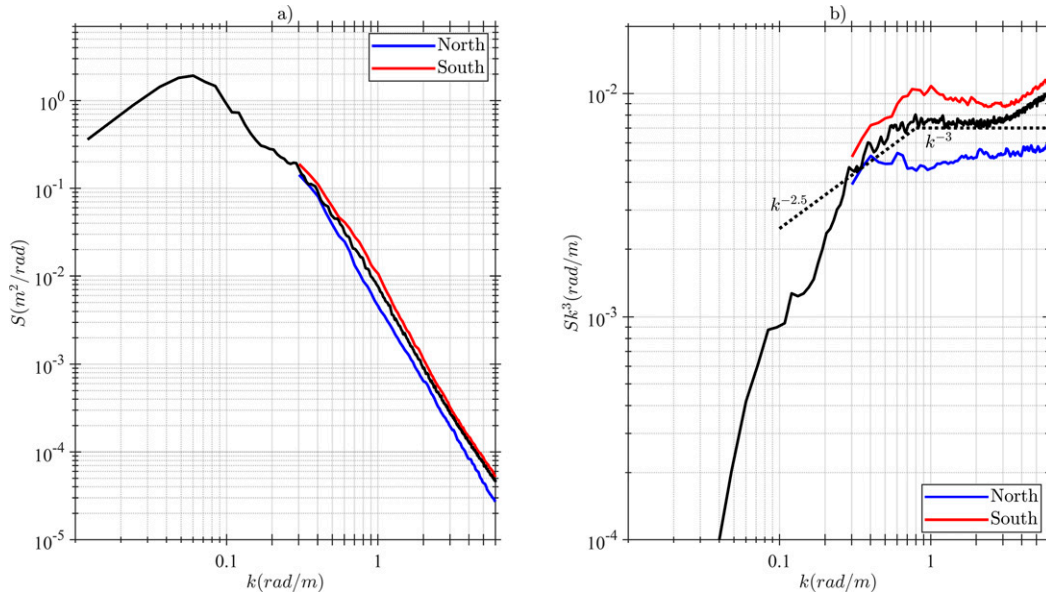


FIG. 8. Averaged (a) omnidirectional spectra and (b) saturation spectra for the east front. The red line represents spectra for the area on the south side of the front ( $n = 30$  m), while the blue line represents spectra for the north side of the front ( $n = -80$  m). As it is not possible to properly resolve lower wavenumbers ( $k < 0.3$ ) with our window size, they are represented using a mean spectrum for the whole area under consideration (black solid line). Note the amplification of higher spectral components ( $k > 0.3$  rad  $m^{-1}$ ) by approximately a factor of 2.

### c. Spectral analysis

To characterize the evolution of surface wave properties as a function of distance from the frontal boundary, directional spectra are computed using two-dimensional fast Fourier transforms (FFT) over data segments  $62.5 \text{ m} \times 62.5 \text{ m}$  with a horizontal resolution of  $0.25 \text{ m}$ . These segments are defined along the entire flight trajectory, and are taken every  $62.5 \text{ m}$  in the along-track direction, and every  $10 \text{ m}$  in the cross-track direction. The  $n$  coordinate of the area is defined as the distance from the center of these segments to the boundary. Note that the aircraft track was following the direction of the frontal boundary during the flight. Before Fourier transforming, the mean surface elevation was subtracted and the data was tapered with a two-dimensional Hanning window and padded with zeros (for details see Lenain and Melville 2017b; Lenain and Pizzo 2020, 2021).

The resulting spectra are then rotated into the mean wind direction ( $\theta = 55^\circ$ ). Finally, the spectra are sorted as a function of distance from the frontal boundary  $n$ , then bin-averaged together for specific ranges of  $n$ . The spectral data above  $k = 6$  rad  $m^{-1}$  are discarded due to instrument noise. Additionally, while this approach allows us to characterize the spatial variability of shorter waves over small scales, we cannot resolve the longer waves ( $> 62.5 \text{ m}$ ). As such, a mean spectrum (bulk spectrum) is computed using larger segments of  $522 \text{ m} \times 522 \text{ m}$ .

## 5. Results

### a. Wave field modulation

Omnidirectional spectra of the surface wave field  $\phi(k)$  are shown in Fig. 8a computed from areas south ( $n = +30 \text{ m}$ ), and

north ( $n = -80 \text{ m}$ ) of the frontal boundary along with an omnidirectional spectrum computed over the entire experimental domain (bulk spectrum) to resolve the longer waves, as described in section 5c. We find that the higher wavenumber portion of the spectra ( $k > 0.3$  rad  $m^{-1}$ ) to the south of the frontal boundary exhibit larger amplitudes as compared to the background spectrum, while those computed on the north side shows a significant decrease over the same range of wavenumbers. The transition from equilibrium to saturation ranges (Lenain and Melville 2017b) is observed in all three cases. Saturation spectra  $\phi(k)k^3$  are shown in Fig. 8b. We find the higher wavenumber portion of the spectra to be strongly amplified near the front, by almost a factor of 2 as compared to the background spectrum.

Spectrograms of omnidirectional and saturation spectra, as a function of distance from the front boundary  $n$ , are shown in Figs. 9b and 9c. For reference, SST as a function of  $n$  is also plotted in Fig. 9a. The spectra remain mostly unchanged to the north of the boundary ( $n < 0 \text{ m}$ ). Closer to the frontal boundary, especially on the south side ( $n > 0 \text{ m}$ ), we observe an increase in spectral magnitude for the higher-frequency components ( $k > 0.3$  rad  $m^{-1}$ ), reaching a saturation maximum for  $n \in [0, 50] \text{ m}$ , corresponding to the area where wave breaking is enhanced. This observed steepening of the wave field (Figs. 8 and 9) and wave breaking enhancement (Fig. 7a) near the frontal boundary are caused by surface waves interacting with the underlying current. Finally, as waves propagate to the south of the boundary the spectral energy levels are reduced to nearly the levels observed far north of the front ( $n = 125 \text{ m}$ ), in the much more spatially uniform portion of the wave field.



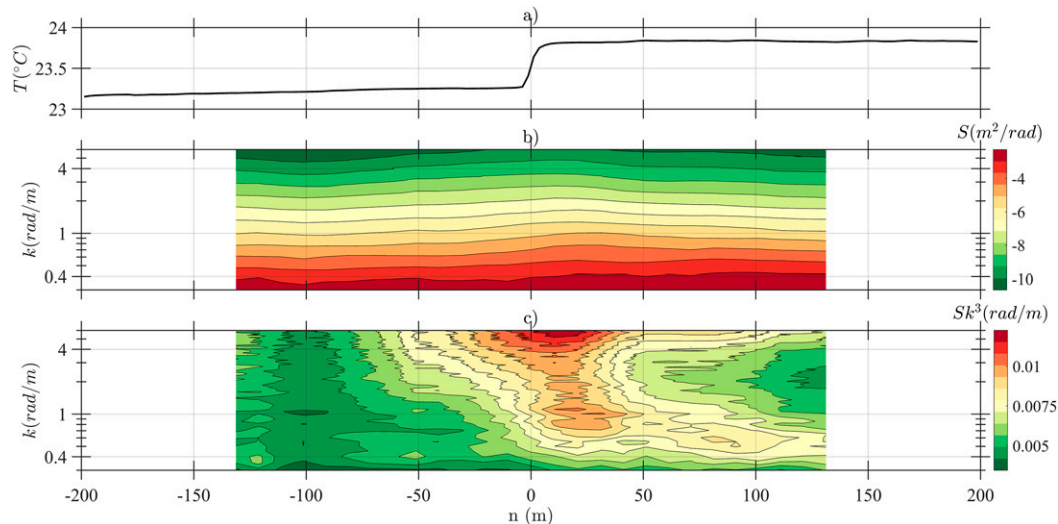


FIG. 9. Evolution of wave spectral properties as a function of distance from the front [(a) temperature is also shown for reference]. A spectrogram of (b) omnidirectional spectra and (c) saturation spectra are calculated for the east portion of the front. The positive side of the abscissa denotes the south side of the front ( $n > 0$ ), and vice versa. The saturation spectra ( $k > 0.3 \text{ rad m}^{-1}$ ) undergoes strong amplification to the south of the front boundary ( $n > 0$ ) with peaks at  $k = 1$  and  $k = 6 \text{ rad m}^{-1}$ .

### b. Active wave breaking statistics

Details about the approach used to compute active wave breaking statistics can be found in the [appendix](#). An example of sea surface imagery showing a large active breaking wave and the corresponding breaking front velocities (red quiver) is shown in [Fig. 10](#).

Omnidirectional  $\Lambda(c_b)$  distributions for elements just to the south of the frontal boundary ( $n \in [0, 30] \text{ m}$ ) and further north ( $n \in [-200, -50] \text{ m}$ ) are shown in [Fig. 11a](#). We find a significant increase in the magnitude of  $\Lambda(c_b)$  between these two regions, by up to two orders of magnitude for  $c_b < 6 \text{ m s}^{-1}$ , while the distributions are approximately the same for higher velocities. These distributions are collected in areas just a few hundred meters apart, again highlighting the sharpness of the front, and the localized effects of the interaction of the waves with the front. Relatively little wave breaking is observed for  $c_b > 10 \text{ m s}^{-1}$ , in line with observations from [Kleiss and Melville \(2011\)](#).

Scaled  $\Lambda(c_b)c_b^4$  distributions, which are related to the momentum flux density due to wave breaking, as defined by Eq. (4), are plotted in [Fig. 11b](#). We find a peak of the distribution around  $c_b = 4 \text{ m s}^{-1}$ , which then decreases to negligible amounts for larger velocities. This decrease in magnitude is more pronounced north of the frontal boundary, with negligible values for  $c_b > 2 \text{ m s}^{-1}$ . The position of this peak ( $c_b = 4 \text{ m s}^{-1}$ ) approximately aligns with the observed increase in surface wave spectral magnitude around  $k = 1 \text{ rad m}^{-1}$  (see [Fig. 8](#)), corresponding to a phase velocity of  $3.1 \text{ m s}^{-1}$ .

The evolution of wave breaking statistics, as a function of distance from the boundary  $n$ , is shown in [Fig. 12](#), along with the observed SST. The whitecap coverage  $W$  is shown in [Fig. 12b](#)

and the zeroth moment of the  $\Lambda(c_b)$  distribution in [Fig. 12c](#). While their magnitude remain small on the north side of the frontal boundary ( $n < 0 \text{ m}$ ), these measures of breaking rapidly increase for  $n > 0 \text{ m}$ , with a maximum value found within 10 m of the frontal boundary, and in general exhibiting larger magnitudes on the south side of the front. A spectrogram of  $\Lambda(c_b)$  is given in [Fig. 12d](#). The distributions are mostly uniform to the north of the boundary ( $n < 0 \text{ m}$ ), then undergo a sharp order of magnitude amplification directly south of the boundary (for breaking velocities lower than approximately  $4 \text{ m s}^{-1}$ ) over just a few meters. Further south of the boundary,  $\Lambda(c_b)$  remained elevated while slowly decreasing away from the front.

### c. Directional properties of the wave field

Directional wavenumber and saturation spectra at the same locations as the omnidirectional spectra plotted in [Fig. 8](#), north and south of the frontal boundary, are shown in [Fig. 13](#). The spectra have been rotated such that the  $x$  axis is aligned with the mean wind direction,  $\theta = 55^\circ$  (coming from true north). Spectra computed north of the boundary are shown in [Figs. 13a](#) and [13b](#), while the spectra to the south of the boundary are shown in [Figs. 13c](#) and [13d](#).

The primary difference between the two spectra is the amplification of the higher wavenumbers south of the front, which is shown most clearly by the saturation spectra. These modulations by the front manifest themselves in both larger amplitudes of the saturation spectra, and a broader directional distribution. In general, an opposing current will focus the wave field—decreasing its directional spread (see the related discussion in [Lenain and Pizzo 2021](#)) and increasing its slope. Here, we see that for  $k \approx 1 \text{ rad m}^{-1}$ , the



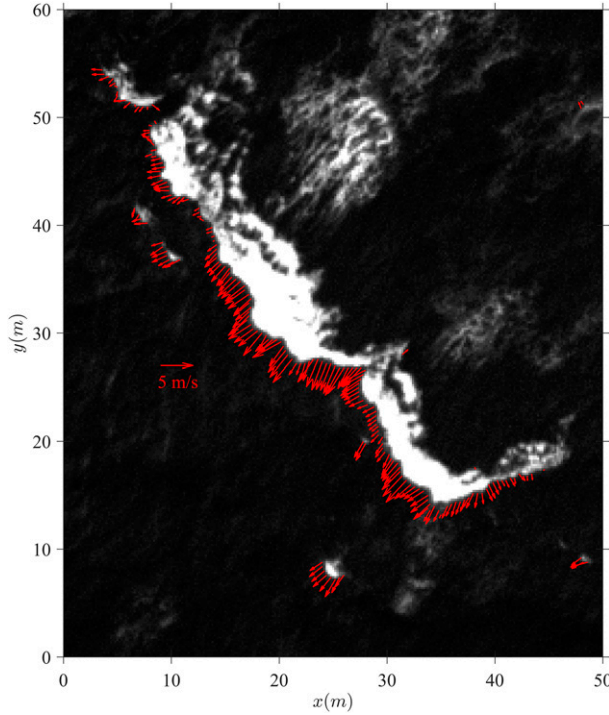


FIG. 10. A georeferenced large-scale breaking wave obtained from the aerial imagery. Actively breaking waves, and their associated velocities [determined using the optical flow method of Liu (2009); see the appendix for details], are plotted by the red arrows. A large number of such images are used to define the  $\Lambda(c_b)$  distribution, which provides a statistical description of wave breaking for the given area.

components south of the front remain relatively narrowly spread. For larger wavenumbers, much larger directional spreading is found.

Directional  $\Lambda(\mathbf{c}_b)$  distributions where  $\mathbf{c}_b = (c_x, c_y)$  for elements just to the south of the frontal boundary ( $n \in [-30, 0]$  m) and to the north ( $n \in [0, 30]$  m) are shown in Figs. 14a and 14b. These distributions are rotated into the mean wind direction (which is the same as the directional spectra presented in Fig. 13). We find significantly more breaking on the south side of the front, especially for  $c_x < 3.5 \text{ m s}^{-1}$  and  $|c_y| < 1.5 \text{ m s}^{-1}$ . We observe a larger number of breakers in the crosswind direction for larger values of  $c_y$  (i.e., longer waves). The magnitude of surface currents is estimated as  $1.04$  and  $0.59 \text{ m s}^{-1}$  (north and south, respectively), with directions of  $95^\circ$  and  $137^\circ$  (coming from true north).

Following the approach of Kleiss and Melville (2011), a first order approximation of surface currents can be obtained from the motion of nonbreaking foam patches. In order for a patch to be considered nonbreaking, we require that at least 99% of the elements of the boundary of the foam patch are classified as nonbreaking. Surface current magnitudes are then computed by tracking the velocity of the foam patches, and are indicated by white cross marks in Fig. 14b.

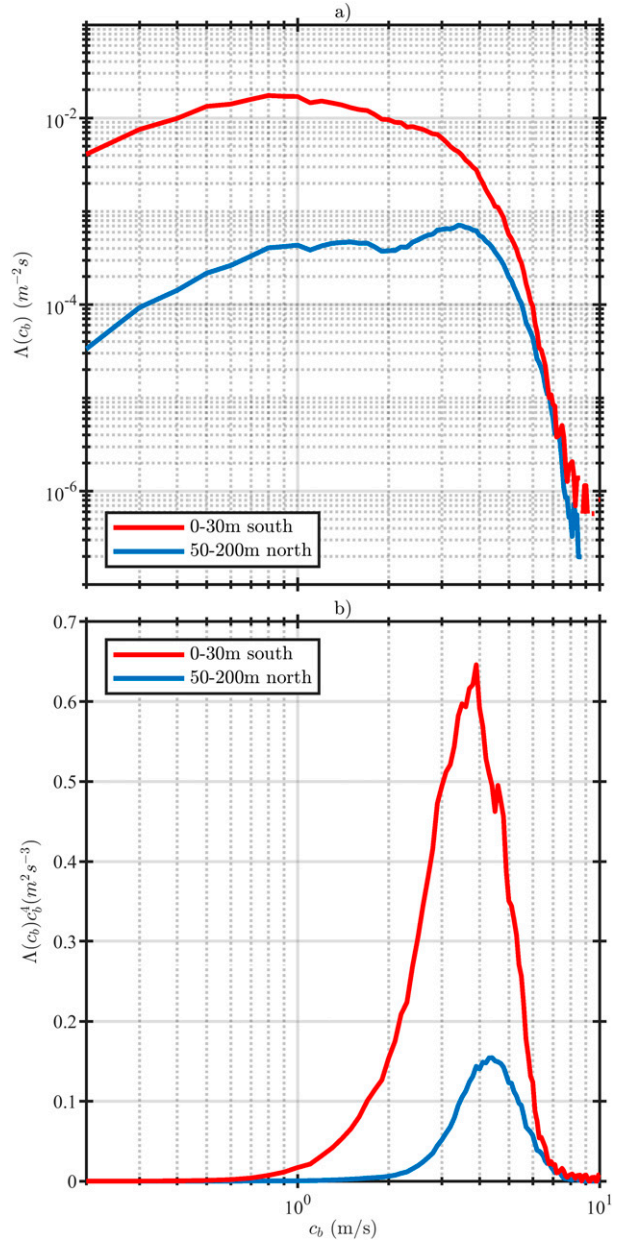


FIG. 11. (a)  $\Lambda(c)$  distributions for the east portion of the front. Results are shown for the area just to the south of boundary ( $0 < n < 30 \text{ m}$ ), and further away to the north of it ( $-50 > n > -200 \text{ m}$ ). (b) As in (a), but the distribution is multiplied by  $c_b^4$  (giving a quantity related to the integrand of the momentum flux). Note that while the greatest amplification of the distribution is for lower velocities (two orders of magnitude), the dynamically most significant section of the distribution is around  $c_b = 4 \text{ m s}^{-1}$  (with amplification by a factor of 5).

#### d. Surface wave induced mass transport

Stokes and wave breaking drift are computed according to Eqs. (2) and (5), respectively, using the directional wave spectrum and breaking distributions. They are then

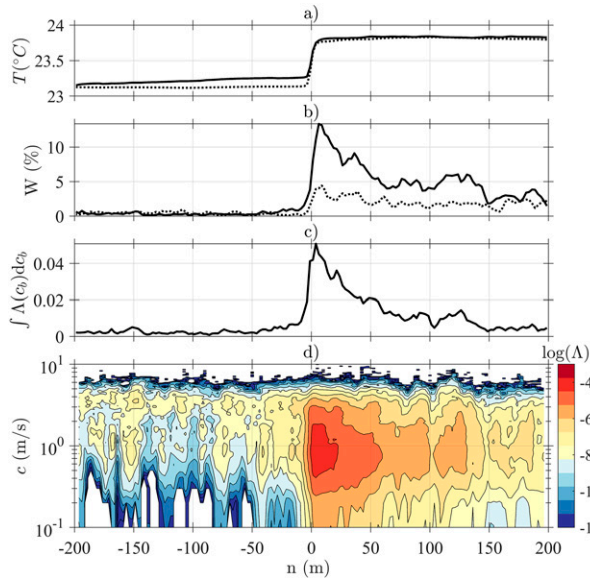


FIG. 12. Wave field parameters as a function of distance from the front. (a) Temperature, (b) whitecap coverage, (c) total  $\Lambda$  distribution, and (d) spectrogram of  $\Lambda(c)$  distribution are shown for the east portion of the front. Results are shown as a function of distance from the frontal boundary, with the positive abscissa ( $n > 0$ ) indicating a region south of the front. The breaking statistics are well correlated with the change of SST, and the amplification of  $\Lambda(c_b)$  distribution (for intermediate and lower velocities), occurs over the distance of a few meters.

conditionally averaged alongfront (i.e., in the  $s$  direction) for each section. Mean surface currents [see Kleiss and Melville (2011) and previous subsection] are shown in Fig. 15a for the east section in the Earth coordinate system. We find that surface currents are rapidly rotating close to the frontal boundary, experiencing close to a  $120^\circ$  change in just 200 m. No surface current estimates were computed on the north side, away from the front, due to limited whitecap coverage. Note, this is an indirect way of inferring surface currents, and should be treated as a first-order estimate.

The corresponding values of Stokes drift are shown in Fig. 15b. The magnitude of the Stokes drift  $\mathbf{U}_s$  at the surface increases just south of the frontal boundary by nearly 50%. The Stokes drift direction is oriented in the mean wind direction north of the frontal boundary ( $n < 0$  m), then rotates in a clockwise direction near the boundary (by approximately  $17^\circ$ ). The wave breaking induced drift  $\mathbf{U}_b$  is given in Fig. 15c. We find that the magnitude of the wave breaking induced drift rapidly increases near the frontal boundary by up to an order of magnitude. The direction of the drift remains approximately constant across the front, aligned with the wind direction. Finally, the ratio between wave breaking induced and Stokes drift is given in Fig. 15d, illustrating the important contribution of the wave breaking induced drift (by up to 100% of the value of the Stokes drift near the frontal

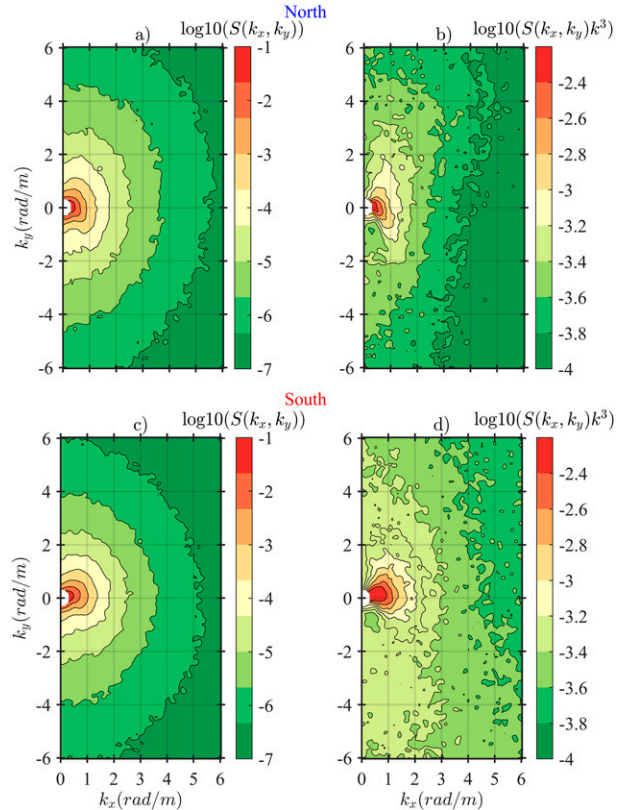


FIG. 13. (a) Directional  $S(k_x, k_y)$  spectra and (b)  $S(k_x, k_y)k^3$  saturation spectra for the north portion of the front. (c), (d) As in (a) and (b), but for south portion of the front. All results are shown for east portion of the front (east of  $x = -2400$  m). The spectra have been rotated into the wind reference frame ( $55^\circ$ , coming from true north), with the  $x$  axis representing mean wind direction. Note the strong refraction (and amplification) of the spectra in (c) and (d).

boundary) to upper-ocean processes in this type of scenario (Pizzo et al. 2019).

#### e. Amplification of the momentum flux near the frontal boundary

From the directional spectra of the surface waves and the  $\Lambda(c_b)$  distribution, we can also estimate the wave-breaking induced momentum flux  $\mathbf{M}$ . This is shown in Fig. 16b plotted as a function of cross front distance  $n$ . The SST is shown in Fig. 16a, for reference. The magnitude of the wave-induced drift is plotted in Fig. 16c. The momentum flux is much smaller on the northern side of the front ( $n < 0$  m). However, near the frontal boundary, for  $0 < n < 50$  m in particular, we find a rapid increase of the momentum flux, by an order of magnitude, reaching a value of  $1 \text{ N m}^{-2}$ .

This is significant, as wave breaking balances the momentum flux from the wind for young waves (Sutherland and Melville 2013, 2015a). That is—nearly all of the momentum

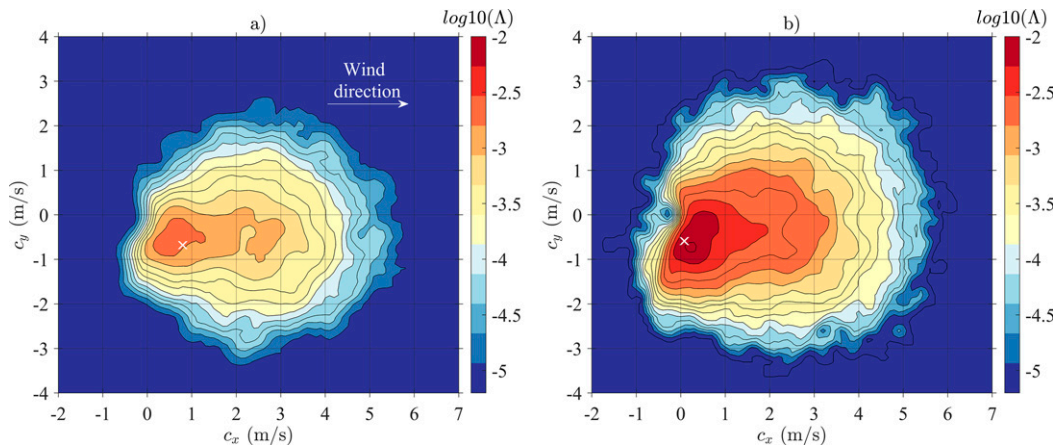


FIG. 14. Directional  $\Lambda(c_1, c_2)$  distributions for area north from the boundary ( $0 < n < -30$ ,  $n$  is distance from boundary in meters), and just to the south of it ( $0 > n > 30$ ). The distribution has been rotated into the wind reference frame ( $55^\circ$ ) from true north, with the  $c_x$  representing velocities in the mean wind direction. The white cross marks indicate the mean inferred surface currents for the area based on the motion of foam patches. In addition to amplification in magnitude, a change of directional properties can be observed to the south of the front.

that is transferred from the wind to the waves goes into wave breaking once the sea surface has been modestly deformed (Banner and Peirson 1998; Grare et al. 2013; Sutherland and Melville 2013, 2015a). Therefore, this localized breaking at the front represents an important conduit for momentum to be transferred indirectly from the wind to the water column. This applies to both the magnitude of the momentum flux as well as its spatial distribution. The measurements provided here should be useful in providing realistic spatial distributions of the momentum flux to be used in coupled air–sea models.

Note that the contribution of nonaerated breakers (i.e., lower velocities) is not included here but could also contribute significantly to the momentum flux (see Sutherland and Melville 2013).

## 6. Discussion and conclusions

In this study, we have presented novel high-resolution airborne remote sensing observations of wave modulation in the vicinity of a submesoscale front near the island of O’ahu, Hawaii. We find enhanced breaking on one side of the front, caused by wave–current interaction processes. This work expands previous studies on this topic (e.g., Romero et al. 2017; Raschle et al. 2018), by characterizing the evolution of surface properties at a much higher spatial resolution, in the area directly near the front (within less than a couple of hundred meters, and with submeter horizontal resolution). Overall, we found that the surface wave field is strongly modulated by the front. This in turn leads to significant spatial inhomogeneities in bulk scale properties of the wave field and wave breaking statistics.

To capture the rapid spatial evolution of these features, especially within a few meters of the frontal boundary, the present analysis was conducted in a “front coordinate system.” We found that currents, breaking statistics, temperature, and spectral properties varied significantly over very short spatial scales (on the order of a few meters).

This in turn rapidly increases the magnitude of Stokes and breaking induced drifts, which are enhanced by around 50% and an order of magnitude, respectively, within a distance of 50 m or less, near the boundary of the front. The breaking induced velocity is particularly large near the frontal boundary, exceeding locally the Stokes drift. This is important, as a significant portion of wind stress is absorbed by the wave field (Banner and Peirson 1998; Grare et al. 2013), which is then transferred to the upper ocean through wave breaking. This process is often assumed to be spatially uniform, at least in the modeling community. This study shows that the distribution of momentum flux due to breaking can vary significantly near fronts, and more broadly in the presence of wave–current interactions. It is also shown that the total wave induced drift can vary by nearly a factor of 2 over the same distance. As the momentum flux from the atmosphere to the ocean and wave averaged effects (drift) can be key components governing the dynamics of submesoscale fronts, this may have significant implications for front stability and frontogenesis (McWilliams 2016). This would in turn affect many other ocean processes (such as vertical flux of nutrients, propagation of near-surface pollutants, and air–sea heat and gas fluxes), which are strongly modulated by submesoscale features. Note that here the gradients of surface velocity (Fig. 15a) across the front are found to significantly exceed  $f$ , the Coriolis force, by more than a factor of 400.



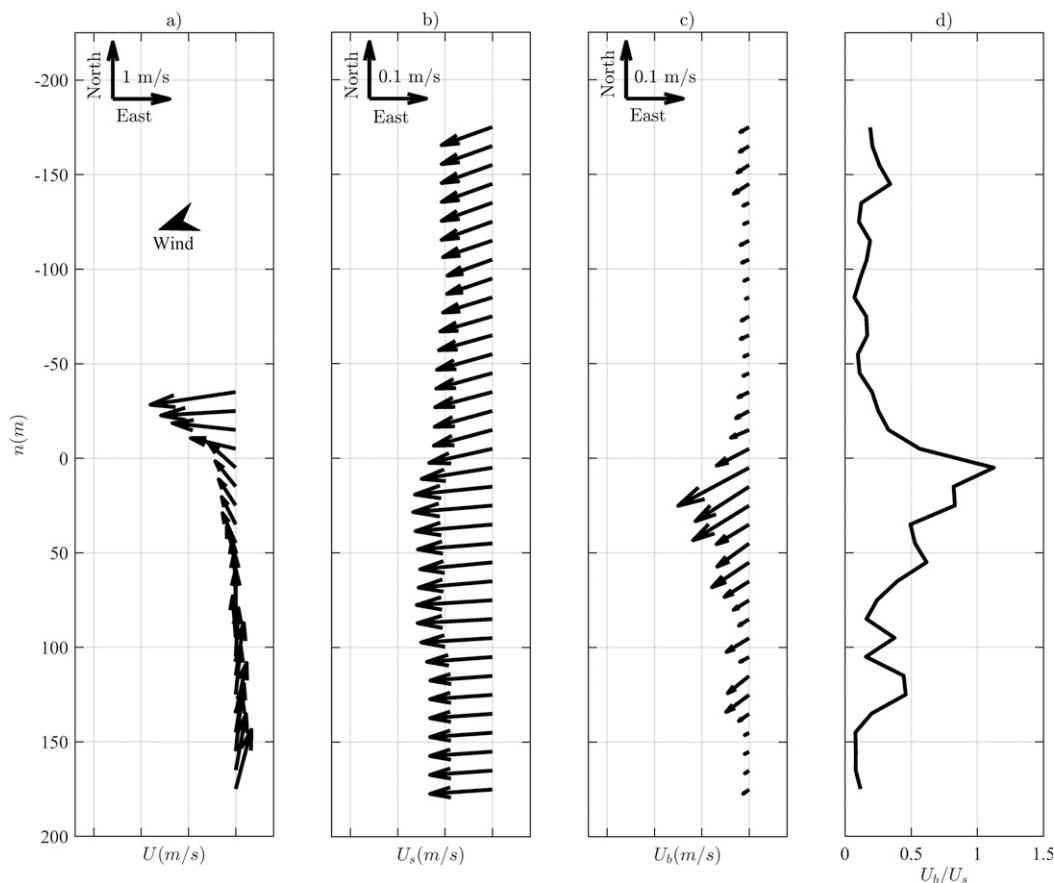


FIG. 15. Observed and derived surface velocities for the east portion of the front ( $x > -2400$  m). Results are shown in the approximate reference frame of the front (rotated by  $25^\circ$ ), where the vertical components of velocities indicate cross-front velocities, and the horizontal components of velocities indicate alongfront velocities. (a) Total surface velocities (black arrows) obtained from whitecap motion. (b) Stokes drift. (c) Breaking induced drift. (d) Ratio of breaking induced and Stokes drifts. All results are shown as a function of distance from the front boundary, with positive abscissa ( $n > 0$ ) indicating south side. The total surface currents undergo a rapid evolution at the frontal boundary, and the value of both drifts is significantly amplified, with the breaking induced drift approaching the magnitude of the Stokes drift.

The results presented in this paper are a step toward better understanding wave–current interactions and wave breaking at a submesoscale front. They also highlight the need for broad spatiotemporal measurements of the atmosphere–ocean boundary layer at these locations. A combination of airborne measurements of sea surface and current measurements (including divergence, vorticity, and its depth profile), performed by autonomous surface vehicles (Lenain and Melville 2014; Grare et al. 2021), would establish the range of magnitudes of submesoscale currents and their spatial variability, which is of crucial importance for the development of new wave models and many of the physical and biological processes. This will be further examined by the authors as part of the NASA S-MODE Earth Venture Suborbital III research program.

**Acknowledgments.** The authors are grateful to Williams Aerial Inc. for providing flight resources. We thank Nick Statom for making the initial observation of the enhanced breaking, and for georeferencing the visible light imagery. We thank Jules Hummon (University of Hawaii) for help with the shipborne data. We thank an anonymous referee and Nicolas Rasle for insightful comments that have led to an improved manuscript. This research was supported by grants from the Physical Oceanography programs at ONR (Grants N00014-17-1-2171, N00014-14-1-0710, and N00014-17-1-3005) NSF (OCE; Grant OCE-1634289), and NASA (Grant 80NSSC19K1688).

**Data availability statement.** All presented data are available at the UCSD Library Digital Collection (<https://doi.org/10.6075/JOFN162S>) and the Rolling Deck to Repository (R2R) for the shipborne data (KOK1801, [Rolling Deck to Repository](#) 2019).

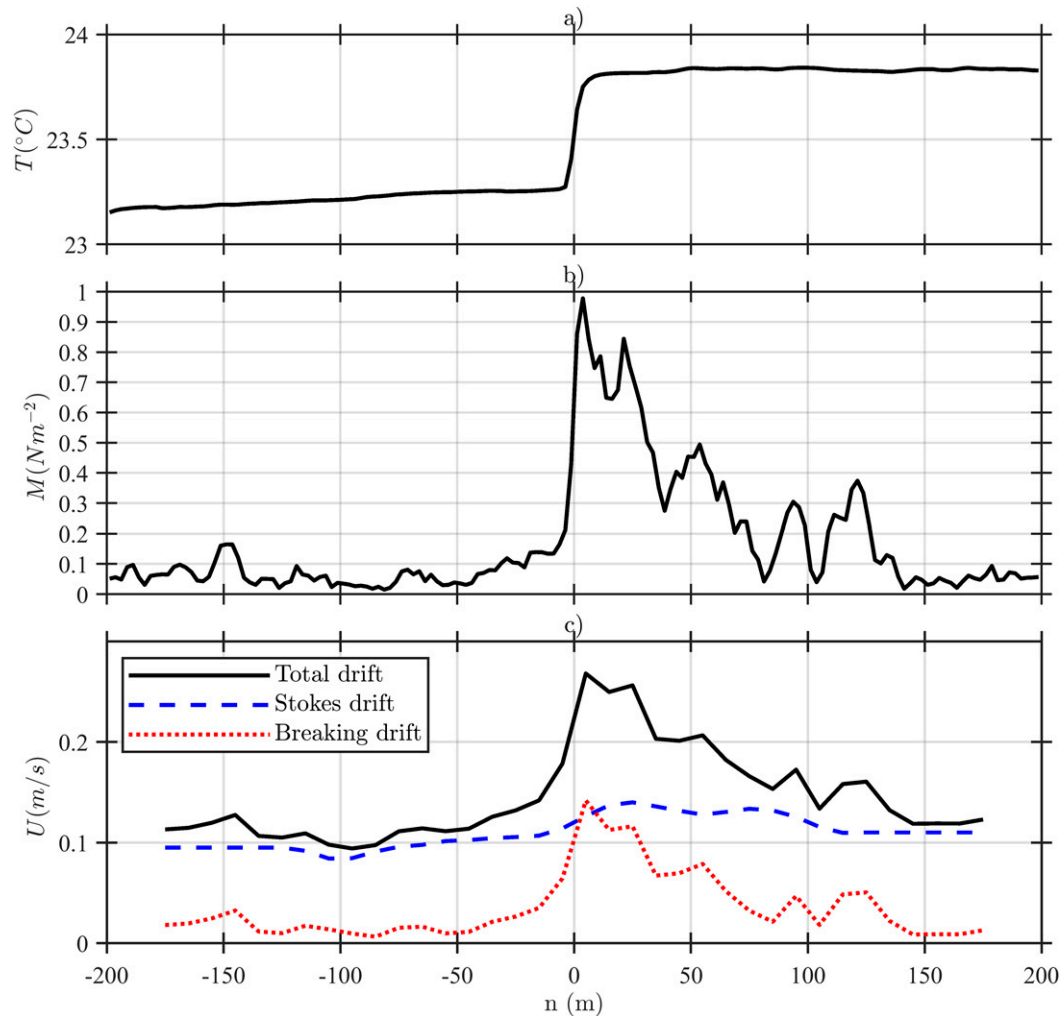


FIG. 16. Distributions of (a) sea surface temperature, (b) momentum flux to the oceans upper layer due to wave breaking, and (c) wave-induced (total, Stokes, and breaking) drifts as a function of distance from the front. Note the spatial inhomogeneity of momentum flux and of wave-induced surface drift. They vary by an order of magnitude and by a factor of 2 at the frontal boundary.

## APPENDIX

### Active Wave Breaking Statistics

Our approach to computing  $\Lambda(\mathbf{c}_b)$  is based on [Kleiss and Melville \(2011\)](#). Observing wave breaking statistics is a notoriously difficult problem, as differentiating foam and actively breaking waves from the sea surface can be particularly challenging ([Kleiss and Melville 2010, 2011](#); [Sutherland and Melville 2013, 2015a,b](#)). First, a normalized complementary cumulative image intensity distribution  $p(i)$  is computed for each georeferenced image where  $i$ , the pixel intensity, varies from 0 (black) to 1 (white). These distributions exhibits two regimes (see [Kleiss and Melville 2011](#)), one dominated by foam and wave breaking patches, and the other corresponding to the underlying unbroken sea surface. By identifying this

transition, using a brightness threshold ( $I_t$ ) defined in [Kleiss and Melville \(2011\)](#) and determined from the second derivative of the natural logarithm of  $p(i)$ , we can characterize the contours of the foam and breaking waves. Here the threshold ( $I_t = 0.021$ ) was set to filter out most foam patches. Additionally, only contours of 5 pixels or more were considered in the analysis.

The motion of whitecaps can be tracked using particle image velocimetry (PIV) methods, with application of the optical flow method for small-scale tuning of velocities [Kleiss and Melville \(2011\)](#). To improve accuracy for areas highly saturated with whitecaps, and for tracking large-scale breakers with variable velocities along its breaking front, a new method of estimating breaker velocities is utilized. The velocity of each contour element is determined using the optical flow methods described by [Liu \(2009\)](#), using pairs of successive

images separated by  $dt = 0.2$  seconds. The method seeks to minimize the energy  $E$  of two subsequent images defined as

$$E \equiv |I_1 - I_2|^2 + \alpha(|\nabla u|^2 + |\nabla v|^2), \quad (\text{A1})$$

where  $I_1$  and  $I_2$  are two subsequent images,  $\alpha$  is a regularization term,  $u$  and  $v$  are computed pixel velocities, and the energy  $E$  is summed over every pixel of the two images. The images are first downsampled to determine large-scale motions, and the resolution is gradually refined in order to determine smaller scale features. More details can be found in Liu (2009), Brox et al. (2004), and Bruhn et al. (2005).

A multichannel image approach is used to include brightness gradient in the analysis. The energy is minimized for the image defined as  $\mathbf{I} = (I, 0.5I_x, 0.5I_y)$  where  $I$  is the original grayscale image, and  $I_x$  and  $I_y$  are its spatial derivatives. The values of derivatives are constrained to be real and positive by subtracting their smallest negative value, and a factor of 0.5 is applied to equalize the weight of the original image and its gradients. The value of the upsampling rate was set to 0.85 and the value of the regularization parameter ( $\alpha$ ) was chosen to take values from 60 to 150 in order to minimize outliers in the obtained velocity  $[(u, v) > 12 \text{ m s}^{-1}]$ , or outliers in velocity gradients ( $|\nabla u| > 6 \text{ Hz}$  or  $|\nabla v| > 6 \text{ Hz}$ ).

The following criteria were used to differentiate active breaking from foam:

- The brightness gradient of the image is above a set threshold.
- The difference of brightness for the same pixel in two subsequent images is above a set level.
- The direction of the velocity of each contour element is  $\pm 110^\circ$  from the mean wind direction.
- The direction of the normal to the contour element is  $\pm 110^\circ$  from the mean wind direction.
- The area of the considered patch needs to increase in each subsequent image. This criterion is applied uniformly for each element of the contour.

It was required that each contour element passes four out of five criteria in order to be considered an active breaker. Furthermore, if any element was found to be propagating into the interior of the foam patch, or if they had no direct neighboring elements which were also registered as actively breaking, they were discarded.

## REFERENCES

- Arduhin, F., S. T. Gille, D. Menemenlis, C. B. Rocha, N. Rasche, B. Chapron, J. Gula, and J. Molemaker, 2017: Small-scale open ocean currents have large effects on wind wave heights. *J. Geophys. Res. Oceans*, **122**, 4500–4517, <https://doi.org/10.1002/2016JC012413>.
- Banner, M. L., and W. L. Peirson, 1998: Tangential stress beneath wind-driven air–water interfaces. *J. Fluid Mech.*, **364**, 115–145, <https://doi.org/10.1017/S0022112098001128>.
- Breivik, Ø., J.-R. Bidlot, and P. A. Janssen, 2016: A Stokes drift approximation based on the Phillips spectrum. *Ocean Modell.*, **100**, 49–56, <https://doi.org/10.1016/j.ocemod.2016.01.005>.
- Bretherton, F. P., and C. J. R. Garrett, 1968: Wavetrains in inhomogeneous moving media. *Proc. Roy. Soc.*, **A302**, 529–554, <https://doi.org/10.1098/rspa.1968.0034>.
- Brox, T., A. Bruhn, N. Papenberg, and J. Weickert, 2004: High accuracy optical flow estimation based on a theory for warping. *Computer Vision - ECCV 2004*, T. Pajdla and J. Matas, Eds., Lecture Notes in Computer Science, Vol. 3024, Springer, 25–36.
- Bruhn, A., J. Weickert, and C. Schnörr, 2005: Lucas/Kanade meets Horn/Schunck: Combining local and global optic flow methods. *Int. J. Comput. Vis.*, **61**, 211–231, <https://doi.org/10.1023/B:VISI.0000045324.43199.43>.
- Callaghan, A. H., and M. White, 2009: Automated processing of sea surface images for the determination of whitecap coverage. *J. Atmos. Oceanic Technol.*, **26**, 383–394, <https://doi.org/10.1175/2008JTECHO634.1>.
- D'Asaro, E. A., and Coauthors, 2018: Ocean convergence and the dispersion of flotsam. *Proc. Natl. Acad. Sci. USA*, **115**, 1162–1167, <https://doi.org/10.1073/pnas.1718453115>.
- Deike, L., N. Pizzo, and W. K. Melville, 2017: Lagrangian transport by breaking surface waves. *J. Fluid Mech.*, **829**, 364–391, <https://doi.org/10.1017/jfm.2017.548>.
- Drazen, D. A., W. K. Melville, and L. Lenain, 2008: Inertial scaling of dissipation in unsteady breaking waves. *J. Fluid Mech.*, **611**, 307–332, <https://doi.org/10.1017/S0022112008002826>.
- Dysthe, K. B., 2001: Refraction of gravity waves by weak current gradients. *J. Fluid Mech.*, **442**, 157–159, <https://doi.org/10.1017/S0022112001005237>.
- Grare, L., L. Lenain, and W. K. Melville, 2013: Wave-coherent airflow and critical layers over ocean waves. *J. Phys. Oceanogr.*, **43**, 2156–2172, <https://doi.org/10.1175/JPO-D-13-056.1>.
- , N. Statom, N. Pizzo, and L. Lenain, 2021: Instrumented wave gliders for air-sea interaction and upper ocean research. *Front. Mar. Sci.*, **8**, 664728, <https://doi.org/10.3389/fmars.2021.664728>.
- Gula, J., M. J. Molemaker, and J. C. McWilliams, 2014: Submesoscale cold filaments in the Gulf Stream. *J. Phys. Oceanogr.*, **44**, 2617–2643, <https://doi.org/10.1175/JPO-D-14-0029.1>.
- Hamlington, P. E., L. P. Van Roekel, B. Fox-Kemper, K. Julien, and G. P. Chini, 2014: Langmuir–submesoscale interactions: Descriptive analysis of multiscale frontal spindown simulations. *J. Phys. Oceanogr.*, **44**, 2249–2272, <https://doi.org/10.1175/JPO-D-13-0139.1>.
- Hoskins, B. J., and F. P. Bretherton, 1972: Atmospheric frontogenesis models: Mathematical formulation and solution. *J. Atmos. Sci.*, **29**, 11–37, [https://doi.org/10.1175/1520-0469\(1972\)029<0011:AFMMFA>2.0.CO;2](https://doi.org/10.1175/1520-0469(1972)029<0011:AFMMFA>2.0.CO;2).
- Kenyon, K. E., 1969: Stokes drift for random gravity waves. *J. Geophys. Res.*, **74**, 6991–6994, <https://doi.org/10.1029/JC074i028p06991>.
- , 1971: Wave refraction in ocean currents. *Deep-Sea Res. Oceanogr. Abstr.*, **18**, 1023–1034, [https://doi.org/10.1016/0011-7471\(71\)90006-4](https://doi.org/10.1016/0011-7471(71)90006-4).
- Kleiss, J. M., and W. K. Melville, 2010: Observations of wave breaking kinematics in fetch-limited seas. *J. Phys. Oceanogr.*, **40**, 2575–2604, <https://doi.org/10.1175/2010JPO4383.1>.
- , and —, 2011: The analysis of sea surface imagery for whitecap kinematics. *J. Atmos. Oceanic Technol.*, **28**, 219–243, <https://doi.org/10.1175/2010JTECHO744.1>.
- Lenain, L., and W. K. Melville, 2014: Autonomous surface vehicle measurements of the ocean's response to tropical cyclone Freda. *J. Atmos. Oceanic Technol.*, **31**, 2169–2190, <https://doi.org/10.1175/JTECH-D-14-00012.1>.



- , and —, 2017a: Evidence of sea-state dependence of aerosol concentration in the marine atmospheric boundary layer. *J. Phys. Oceanogr.*, **47**, 69–84, <https://doi.org/10.1175/JPO-D-16-0058.1>.
- , and —, 2017b: Measurements of the directional spectrum across the equilibrium saturation ranges of wind-generated surface waves. *J. Phys. Oceanogr.*, **47**, 2123–2138, <https://doi.org/10.1175/JPO-D-17-0017.1>.
- , and N. Pizzo, 2020: The contribution of high-frequency wind-generated surface waves to the Stokes drift. *J. Phys. Oceanogr.*, **50**, 3455–3465, <https://doi.org/10.1175/JPO-D-20-0116.1>.
- , and —, 2021: Modulation of surface gravity waves by internal waves. *J. Phys. Oceanogr.*, **51**, 2735–2748, <https://doi.org/10.1175/JPO-D-20-0302.1>.
- , N. M. Statom, and W. K. Melville, 2019: Airborne measurements of surface wind and slope statistics over the ocean. *J. Phys. Oceanogr.*, **49**, 2799–2814, <https://doi.org/10.1175/JPO-D-19-0098.1>.
- Lévy, M., P. J. Franks, and K. S. Smith, 2018: The role of submesoscale currents in structuring marine ecosystems. *Nat. Commun.*, **9**, 4758, <https://doi.org/10.1038/s41467-018-07059-3>.
- Liu, C., 2009: Beyond pixels: Exploring new representations and applications for motion analysis. Ph.D. thesis, Massachusetts Institute of Technology, 164 pp.
- Longuet-Higgins, M. S., and R. Stewart, 1964: Radiation stresses in water waves; a physical discussion, with applications. *Deep-Sea Res. Oceanogr. Abstr.*, **11**, 529–562, [https://doi.org/10.1016/0011-7471\(64\)90001-4](https://doi.org/10.1016/0011-7471(64)90001-4).
- Mahadevan, A., 2016: The impact of submesoscale physics on primary productivity of plankton. *Annu. Rev. Mar. Sci.*, **8**, 161–184, <https://doi.org/10.1146/annurev-marine-010814-015912>.
- McWilliams, J. C., 2016: Submesoscale currents in the ocean. *Proc. Roy. Soc.*, **A472**, 20160117, <https://doi.org/10.1098/rspa.2016.0117>.
- , 2017: Submesoscale surface fronts and filaments: Secondary circulation, buoyancy flux, and frontogenesis. *J. Fluid Mech.*, **823**, 391–432, <https://doi.org/10.1017/jfm.2017.294>.
- , 2018: Surface wave effects on submesoscale fronts and filaments. *J. Fluid Mech.*, **843**, 479–517, <https://doi.org/10.1017/jfm.2018.158>.
- Melville, W. K., F. Veron, and C. J. White, 2002: The velocity field under breaking waves: Coherent structures and turbulence. *J. Fluid Mech.*, **454**, 203–233, <https://doi.org/10.1017/S0022112001007078>.
- , L. Lenain, D. R. Cayan, M. Kahru, J. P. Kleissl, P. F. Linden, and N. M. Statom, 2016: The modular aerial sensing system. *J. Atmos. Oceanic Technol.*, **33**, 1169–1184, <https://doi.org/10.1175/JTECH-D-15-0067.1>.
- Peregrine, D., 1999: Large-scale vorticity generation by breakers in shallow and deep water. *Eur. J. Mech. B Fluids*, **18**, 403–408, [https://doi.org/10.1016/S0997-7546\(99\)80037-5](https://doi.org/10.1016/S0997-7546(99)80037-5).
- Phillips, O. M., 1966: *The Dynamics of the Upper Ocean*. Cambridge University Press, 261 pp.
- , 1985: Spectral and statistical properties of the equilibrium range in wind-generated gravity waves. *J. Fluid Mech.*, **156**, 505–531, <https://doi.org/10.1017/S0022112085002221>.
- Pizzo, N., and W. K. Melville, 2013: Vortex generation by deep-water breaking waves. *J. Fluid Mech.*, **734**, 198–218, <https://doi.org/10.1017/jfm.2013.453>.
- , and R. Salmon, 2021: Particle description of the interaction between wave packets and point vortices. *J. Fluid Mech.*, **925**, A32, <https://doi.org/10.1017/jfm.2021.661>.
- , L. Deike, and W. K. Melville, 2016: Current generation by deep-water breaking waves. *J. Fluid Mech.*, **803**, 275–291, <https://doi.org/10.1017/jfm.2016.469>.
- , W. K. Melville, and L. Deike, 2019: Lagrangian transport by nonbreaking and breaking deep-water waves at the ocean surface. *J. Phys. Oceanogr.*, **49**, 983–992, <https://doi.org/10.1175/JPO-D-18-0227.1>.
- Poje, A. C., and Coauthors, 2014: Submesoscale dispersion in the vicinity of the Deepwater Horizon spill. *Proc. Natl. Acad. Sci. USA*, **111**, 12 693–12 698, <https://doi.org/10.1073/pnas.1402452111>.
- Rapp, R. J., and W. K. Melville, 1990: Laboratory measurements of deep-water breaking waves. *Philos. Trans. Roy. Soc.*, **A331**, 735–800, <https://doi.org/10.1098/rsta.1990.0098>.
- Raschle, N., F. Noguier, B. Chapron, and F. J. Ocampo-Torres, 2018: Sun glint images of current gradients at high resolution: Critical angle and directional observing strategy. *Remote Sens. Environ.*, **216**, 786–797, <https://doi.org/10.1016/j.rse.2018.06.011>.
- , and Coauthors, 2020: Monitoring intense oceanic fronts using sea surface roughness: Satellite, airplane, and in situ comparison. *J. Geophys. Res. Oceans*, **125**, e2019JC015704, <https://doi.org/10.1029/2019JC015704>.
- Rolling Deck to Repository, 2019: Cruise KOK1801 on RV Ka'imikai-O-Kanaloa. Rolling Deck to Repository (R2R) Program, <http://www.rvdata.us/catalog/KOK1801>.
- Romero, L., W. K. Melville, and J. M. Kleiss, 2012: Spectral energy dissipation due to surface wave breaking. *J. Phys. Oceanogr.*, **42**, 1421–1444, <https://doi.org/10.1175/JPO-D-11-072.1>.
- , D. Hypolite, and J. C. McWilliams, 2020: Submesoscale current effects on surface waves. *Ocean Modell.*, **153**, 101662, <https://doi.org/10.1016/j.ocemod.2020.101662>.
- , L. Lenain, and W. K. Melville, 2017: Observations of surface wave–current interaction. *J. Phys. Oceanogr.*, **47**, 615–632, <https://doi.org/10.1175/jpo-d-16-0108.1>.
- Shrira, V. I., and A. V. Slunyaev, 2014: Trapped waves on jet currents: Asymptotic modal approach. *J. Fluid Mech.*, **738**, 65–104, <https://doi.org/10.1017/jfm.2013.584>.
- Sinnis, J., L. Grare, L. Lenain, and N. Pizzo, 2021: Laboratory studies of the role of bandwidth in surface transport and energy dissipation of deep-water breaking waves. *J. Fluid Mech.*, **927**, A5, <https://doi.org/10.1017/jfm.2021.734>.
- Srinivasan, K., J. C. McWilliams, M. J. Molemaker, and R. Barkan, 2019: Submesoscale vortical wakes in the lee of topography. *J. Phys. Oceanogr.*, **49**, 1949–1971, <https://doi.org/10.1175/JPO-D-18-0042.1>.
- Stansell, P., and C. MacFarlane, 2002: Experimental investigation of wave breaking criteria based on wave phase speeds. *J. Phys. Oceanogr.*, **32**, 1269–1283, [https://doi.org/10.1175/1520-0485\(2002\)032<1269:EIOWBC>2.0.CO;2](https://doi.org/10.1175/1520-0485(2002)032<1269:EIOWBC>2.0.CO;2).
- Su, Z., J. Wang, P. Klein, A. F. Thompson, and D. Menemenlis, 2018: Ocean submesoscales as a key component of the global heat budget. *Nat. Commun.*, **9**, 775, <https://doi.org/10.1038/s41467-018-02983-w>.
- Sullivan, P. P., and J. C. McWilliams, 2018: Frontogenesis and frontal arrest of a dense filament in the oceanic surface boundary layer. *J. Fluid Mech.*, **837**, 341–380, <https://doi.org/10.1017/jfm.2017.833>.
- , —, and W. K. Melville, 2007: Surface gravity wave effects in the oceanic boundary layer: Large-eddy simulation with vortex force and stochastic breakers. *J. Fluid Mech.*, **593**, 405–452, <https://doi.org/10.1017/S002211200700897X>.

- Sutherland, P., and W. K. Melville, 2013: Field measurements and scaling of ocean surface wave-breaking statistics. *Geophys. Res. Lett.*, **40**, 3074–3079, <https://doi.org/10.1002/grl.50584>.
- , and —, 2015a: Field measurements of surface and near-surface turbulence in the presence of breaking waves. *J. Phys. Oceanogr.*, **45**, 943–965, <https://doi.org/10.1175/JPO-D-14-0133.1>.
- , and —, 2015b: Measuring turbulent kinetic energy dissipation at a wavy sea surface. *J. Atmos. Oceanic Technol.*, **32**, 1498–1514, <https://doi.org/10.1175/JTECH-D-14-00227.1>.
- Suzuki, N., B. Fox-Kemper, P. E. Hamlington, and L. P. Van Roekel, 2016: Surface waves affect frontogenesis. *J. Geophys. Res. Oceans*, **121**, 3597–3624, <https://doi.org/10.1002/2015JC011563>.
- Thomas, L. N., and C. M. Lee, 2005: Intensification of ocean fronts by down-front winds. *J. Phys. Oceanogr.*, **35**, 1086–1102, <https://doi.org/10.1175/JPO2737.1>.
- Villas Bôas, A. B., B. D. Cornuelle, M. R. Mazloff, S. T. Gille, and F. Ardhuin, 2020: Wave–current interactions at meso- and submesoscales: Insights from idealized numerical simulations. *J. Phys. Oceanogr.*, **50**, 3483–3500, <https://doi.org/10.1175/JPO-D-20-0151.1>.
- Yu, L., and R. A. Weller, 2007: Objectively analyzed air–sea heat fluxes for the global ice-free oceans (1981–2005). *Bull. Amer. Meteor. Soc.*, **88**, 527–540, <https://doi.org/10.1175/BAMS-88-4-527>.